Acta Astronautica 202 (2023) 104–118

Contents lists available at ScienceDirect

Acta Astronautica

journal homepage: www.elsevier.com/locate/actaastro

Research paper

A Flagship-class Uranus Orbiter and Probe mission concept using aerocapture

Athul Pradeepkumar Girija[1]

7050 W. Cedar Ave. 101, Lakewood, CO, 80226, United States of America

ARTICLE INFO

Dataset link: https://amat.readthedocs.io/en/master/acta-astronautica.html#uranus-orbiter-and-probe

Keywords:
Uranus
Orbiter
Probe
Flagship-class mission
Aerocapture

ABSTRACT

The conceptual design for a Flagship-class Uranus Orbiter and Probe (UOP) mission using aerocapture is presented. Uranus is historically the least studied destination for aerocapture, primarily attributed to the lack of an engineering-level atmosphere model until UranusGRAM was released by NASA in 2021. The present study is the first detailed end-to-end study of a Uranus aerocapture mission concept taking into account constraints arising from launch vehicle performance, interplanetary trajectory, aerocapture vehicle design, thermal protection system, and probe delivery. The mission concept uses a Falcon Heavy Expendable launcher and a high-energy, fast-arrival V_∞ Earth–Earth–Jupiter–Uranus (EEJU) gravity assist trajectory to deliver a 1400 kg orbiter and a 300 kg entry probe to Uranus. The aerocapture vehicle is a derivative of the Mars Science Laboratory entry system with extensive flight heritage, and uses the state-of-the-art HEEET thermal protection system. Compared to the current baseline UOP mission using conventional propulsive orbit insertion with a 13-year flight time and 5-year orbital mission at Uranus, the proposed 8-year aerocapture mission concept enables a 10-year orbital mission at Uranus within the budgetary and schedule constraints of a Flagship-class mission.

1. Introduction

The ice giants Uranus and Neptune represent a unique class of planets in the Solar System that have not yet been studied by orbiter spacecraft but hold important clues about the formation and evolution of our Solar System. In contrast to the terrestrial inner planets which are mainly composed of rock and the gas giant planets made of hydrogen and helium, the ice giants are mainly composed of planetary ices such as water, ammonia, and methane making them fundamentally different from the inner planets and the gas giants [1–3]. The 2013–2022 Planetary Science Decadal Survey (PSDS) had ranked the Uranus Orbiter and Probe (UOP) as the third-highest priority Flagship-class mission, after Mars Sample Return and the Jupiter Europa orbiter mission [4]. With the first phase of Mars sample return underway by the Mars 2020 rover collecting rock samples and the Europa Clipper mission under construction, the 2023–2032 PSDS has recommended the UOP as the highest priority Flagship-class mission for the next decade [5]. Uranus' large heliocentric distance (19 AU) presents significant mission design challenges for delivering orbiter spacecraft using existing launch vehicles which fit within the budgetary constraints of a Flagship mission [6,7]. In addition, the trajectory must have a reasonable transit time to minimize operational cost and complexity, maximize the duration of the orbital tour, and maximize the radioisotope thermoelectric generator (RTG) power available for the science phase, since their power output decreases with time and limits the total mission life [8]. The 2023–2032 PSDS has baselined a UOP mission with 13-year transit using conventional propulsive insertion and an 18-year total mission [9]. Aerocapture, a technique which uses atmospheric drag from a single pass through the atmosphere to decelerate the spacecraft and achieve nearly fuel-free orbit insertion has been proposed as an alternative to propulsive insertion for all atmosphere-bearing bodies including Uranus [10,11]. The NASA Ice Giants Pre-Decadal mission study concluded aerocapture could allow trip times to be shortened, delivered mass to be increased, and allow the use of less expensive launch vehicles for Uranus and Neptune missions [12].

Fig. 1 shows the number of aerocapture related publications since the 1960s, with studies specifically addressing aerocapture at Uranus shown in light green. The earliest Uranus aerocapture analysis in the literature is a two-part generic aerocapture study performed in 1980 by the General Electric (GE) Co. for the Jet Propulsion Laboratory (JPL) [13], and was later published by Florence [14]. The study developed a generic aerocapture vehicle concept with high lift-to-drag ratio (L/D) of 1.0–2.0 with applications for the Mars Sample Return (MSR), Titan/Saturn Orbiter Dual Probe (S02P), and Uranus Orbiter Probe missions. In 1984, Hoffman extended the results of the GE study and performed a comparison of aerobraking and aerocapture techniques [15]. In 2005, Hall et al. performed a study to

E-mail address: athulpg007@gmail.com.
[1] Independent Consultant

https://doi.org/10.1016/j.actaastro.2022.10.005
Received 22 June 2022; Received in revised form 8 September 2022; Accepted 4 October 2022
Available online 10 October 2022

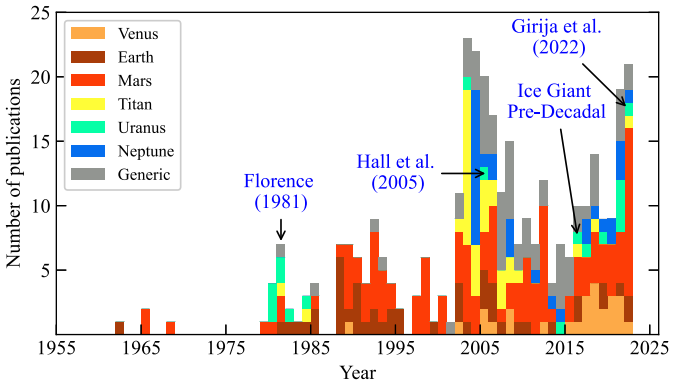

Fig. 1. Number of publications related to aerocapture over the past six decades, with those specifically addressing Uranus shown in light green. Some key studies are annotated. Data available at https://github.com/athulpg007/AMAT/tree/master/bibliometric-data. (For interpretation of the references to color in this figure legend, the reader is referred to the web version of this article.)

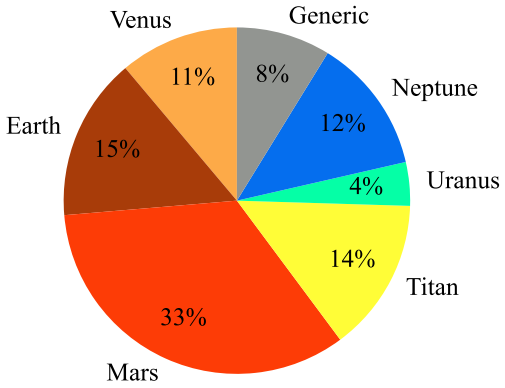

Fig. 2. Pie chart showing the distribution of aerocapture studies for various planets. Uranus aerocapture studies account for only about 4% of the total aerocapture literature.

quantify the cost and delivered mass advantages of aerocapture at all atmosphere-bearing destinations including Uranus [16]. The study found that compared to propulsive orbit insertion, aerocapture can deliver 218% more mass to a 4000 × 450,000 km Uranus orbit. However, the study did not include aerocapture vehicle design and TPS considerations.

In 2014, Agrawal et al. performed an atmospheric entry probe study and explored the use of a mid-L/D aeroshell for aerocapture at Uranus [17]. In 2015, NASA performed a study to determine the status of aerocapture technologies and assess their readiness for missions to Uranus and Neptune [18]. The study concluded that aerocapture can be used at Uranus and Neptune to reduce the time of flight and increase science payload. The study also noted that of all potential solar system destinations, the ice giant planets with their large heliocentric distances stand to benefit the most from using aerocapture. The study concluded that additional studies are required to quantify achievable flight path angle errors at Uranus and Neptune from approach navigation accuracy and ephemeris uncertainties. In 2016, Saikia et al. performed an assessment of aerocapture at Uranus and Neptune in support of the NASA Ice Giants Pre-Decadal (IGPD) survey mission study [19]. The study concluded that unless navigation and atmospheric uncertainties are reduced below currently available estimates then, development of a mid-L/D vehicle would be required for aerocapture at Uranus and Neptune. The IGPD mission study identified aerocapture as a technology that could have an impact on the performance and/or cost of the mission [12]. The study concluded that aerocapture technology could enable trip times to be shortened, delivered mass to be increased or both. Girija et al. performed a study which explored the trade space of high energy short time of flight trajectories to Uranus and Neptune using aerocapture considering the coupled nature of interplanetary trajectory and aerocapture vehicle design [20,21]. The study showed that fast-arrival V_∞ trajectories are better suited for aerocapture as they offer more control authority compared to slow arrival V_∞ and reduce the vehicle L/D requirement. In 2019, a JPL study explored the use of drag modulation aerocapture at Uranus using a deployable entry system [22]. Lubey et al. performed a study of autonomous optical navigation to quantify the achievable EFPA errors at Uranus for aerocapture [23]. Girija et al. performed a quantitative and comparative assessment of aerocapture at all atmosphere-bearing destinations, and showed aerocapture at Uranus is viable with heritage low-L/D aeroshells for certain high arrival V_∞ trajectories [24].

Fig. 2 shows the distribution of aerocapture studies for various Solar System targets. The majority of aerocapture studies have Mars (33%), Earth (15%), and Titan (14%) as their primary targets. Uranus is the least studied destination, accounting for only 4% of the total literature. This is primarily attributed due to the fact that the Aerocapture Systems Analysis Team (ASAT) studies in the early 2000s chose Neptune as a representative target for outer planet aerocapture missions [25]. An outer planet Global Reference Atmospheric Model (GRAM) was developed for Neptune to support the ASAT study, but there was no commonly accepted engineering model for Uranus until 2021. The lack of an engineering atmospheric model and its uncertainties is believed to the major reason why Uranus aerocapture remained less studied than Neptune. In 2021, NASA released the first version of UranusGRAM as part of the GRAM model upgrades which provides an engineering model for the variability, uncertainties, and random perturbations in Uranus' atmosphere. [26].

Despite the significant advantages of aerocapture for outer planet missions, there currently exists no end-to-end study for a Flagship-class orbiter and probe to Uranus using aerocapture. The lack of an end-to-end mission concept study using aerocapture implies scientists and mission planners do not have readily available reference information when performing early mission studies to compare aerocapture with propulsive insertion architectures, and hence aerocapture at Uranus is often not considered during such studies [6,12,27–29].

Aerocapture mission studies must consider multiple disciplines such as launch vehicle performance, interplanetary trajectory, aerocapture vehicle design, and probe delivery to realize a feasible mission concept. The various interdependencies involved between multiple disciplines makes aerocapture mission studies resource intensive, and hence often not viable for budget constrained mission concept studies. The study uses the framework and the Aerocapture Mission Analysis Tool (AMAT) developed at Purdue University for rapid conceptual design of aerocapture missions [30,31]. The present study aims to provide the planetary science community with a Flagship-class mission concept to Uranus using aerocapture which may serve as a benchmark for comparison with propulsive insertion architectures and other potential future aerocapture studies.

2. Mission requirements and constraints

The high-level mission objective is to deliver an orbiter and probe to Uranus within the budgetary and schedule constraints of a Flagship mission. The orbiter and probe mass are roughly the same as that of the UOP mission baselined in the 2023–2032 PSDS mission study [9]. The mission requirements are as follows:

1. The mission must have launch date between 2028 and 2038, and arrive at Uranus no later than 8 years after launch to fit within the schedule.
2. The highest capability launch vehicle available is the Falcon Heavy Expendable (no stages recovered) to fit within the Flagship-class budget.

3. The nominal orbiter (wet mass at the beginning of the orbital phase) and probe mass (at atmospheric entry) is 1400 kg and 300 kg respectively.
4. The launch vehicle must have a launch capability of at least 5000 kg, not including any margin. (Assume the useful payload mass delivered to orbit is 50% of the aerocapture entry system mass, of which 25% is structural mass and 25% is thermal protection system mass. Assume the nominal aerocapture entry system mass is 3600 kg. Assume the cruise stage including propellant for deep space maneuvers weighs 1400 kg. These numbers are to be used for the initial design iteration may be adjusted during the design, as more information becomes available.)
5. To fit within the budget of a Flagship-class mission, the aerocapture entry system must use a Mars Science Laboratory (MSL) derived aeroshell with flight heritage, and has a maximum allowable L/D of 0.24.
6. The mission design must allow at least 1 deg. of theoretical corridor width (TCW) at Uranus. (Assume nominal 3σ EFPA error = ±0.30 deg.)
7. The maximum deceleration load for aerocapture is not to exceed 12 g, based on the MSL entry system design peak deceleration.
8. The maximum stagnation-point peak heat rate is not to exceed 2000 W/cm^2, to enable the use of NASA's Heatshield for Extreme Environment Technology (HEEET) thermal protection system.
9. The maximum stagnation-point total heat load for aerocapture vehicle is not to exceed 350 kJ/cm^2 to limit the TPS mass fraction.
10. The mission must place the orbiter into a 4000 × 550,000 km polar orbit just outside the orbit of Oberon, after which the probe must be delivered.

3. Trade space exploration and baseline mission concept

The selection of a baseline interplanetary trajectory for aerocapture requires consideration of the following factors: (1) the trajectory must allow sufficient launch capability (5000 kg) with a Falcon Heavy Expendable launcher, (2) the trajectory time of flight must not exceed 8 years, and (3) the trajectory arrival V_∞ must allow for sufficient theoretical corridor width (TCW) and satisfy the deceleration, peak heat rate and total heat load constraints. Fig. 3 shows a lift modulation aerocapture feasibility chart for Uranus [24], a graphical method for aerocapture mission design with contours of TCW, peak g-load, peak heat rate $\dot{q}$, and total heat load Q [32]. The vehicle ballistic coefficient β = 146 kg/m^2 and nose radius R_N = 1.125 m are chosen based on the MSL entry system. The dotted horizontal line indicates the maximum allowable L/D = 0.24, assuming an MSL-derived aeroshell. Fig. 3 shows that to achieve the required 1 deg. TCW, the trajectory arrival V_∞ must be at least 20 km/s. To keep the peak heat rate within 2000 W/cm^2 the arrival V_∞ must not exceed about 22 km/s. The initial baseline design (V_∞ = 20.5 km/s, L/D = 0.24) is indicated by the red star which allows 1 deg TCW, keeps the peak g-load under 12 g, the peak heat rate under 2000 W/cm^2, and the total heat load under 350 kJ/cm^2.

A set of high energy, fast arrival V_∞ trajectories computed at JPL and made available to Purdue University during the IGPD study is used as the trajectory dataset for this study. Fig. 4 shows the launch mass capability using the Falcon Heavy Expendable for these high energy trajectories with launch dates between 2026 and 2038. There exists a small set of trajectories which satisfy the required launch mass capability constraint of 5000 kg for launch dates between 2028 and 2032. From this set, the ones that also satisfy the time of flight constraint (TOF < 8 years) and the arrival V_∞ constraint are feasible interplanetary trajectories for an aerocapture mission.

Fig. 5 shows the launch capability on the Falcon Heavy launcher, time of flight, and the arrival V_∞ of the interplanetary trajectory dataset

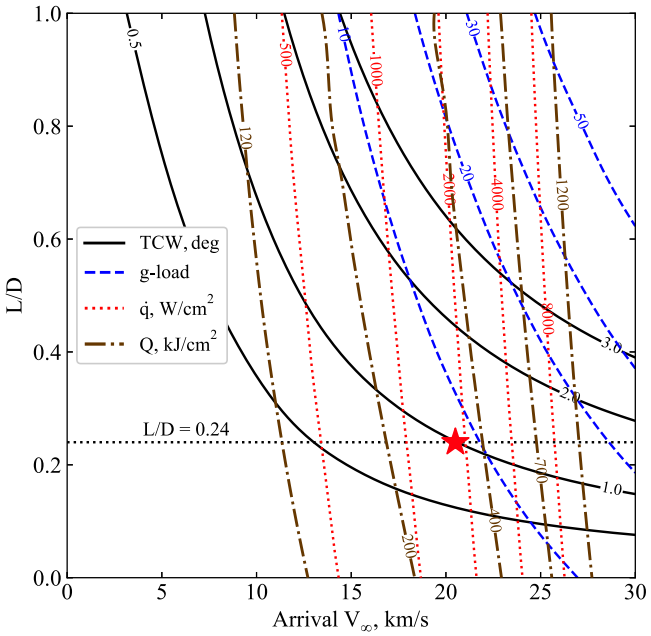

Fig. 3. Uranus lift modulation aerocapture feasibility chart, β = 146 kg/m^2, R_N = 1.125 m. The initial baseline design (V_∞ = 20.5 km/s, L/D = 0.24) is indicated by the red star.

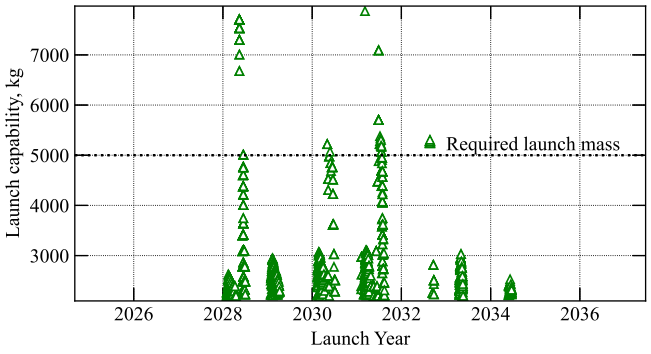

Fig. 4. Falcon Heavy Expendable launch mass capability for high energy trajectories between 2026 and 2038. The dotted line indicates the required 5000 kg launch mass capability.

used in the study. The trajectories in the top left quadrant satisfy the launch mass constraint and the time of flight constraint. A trajectory with V_∞ = 20.5 km/s which also satisfies the V_∞ constraint is selected as the initial baseline trajectory for the study. The selected baseline is an EEJU gravity-assist trajectory with one deep-space maneuver (DSM). The 7.8-year trajectory with C_3 = 53.866 km^2/s^2 provides a launch mass capability of 5069 kg on the Falcon Heavy Expendable. The mission launches on 2031-07-22, performs an Earth flyby on 2034-05-16, Jupiter flyby on 2035-09-04, and arrives at Uranus on 2039-05-18. The DSM ΔV is 1.04 km/s. The arrival V_∞ vector in the International Celestial Reference Frame (ICRF) is [−9.6252, 16.5119, 7.4649] km/s and the arrival declination relative to Uranus' equatorial plane is −48.89 degrees.

4. Approach trajectory and atmospheric entry conditions

Starting with the arrival V_∞ vector, the hyperbolic approach trajectory of the aerocapture vehicle until atmospheric entry interface is computed using the method developed by Hughes [33]. The atmospheric entry interface is defined at 1000 km above the 1 bar pressure

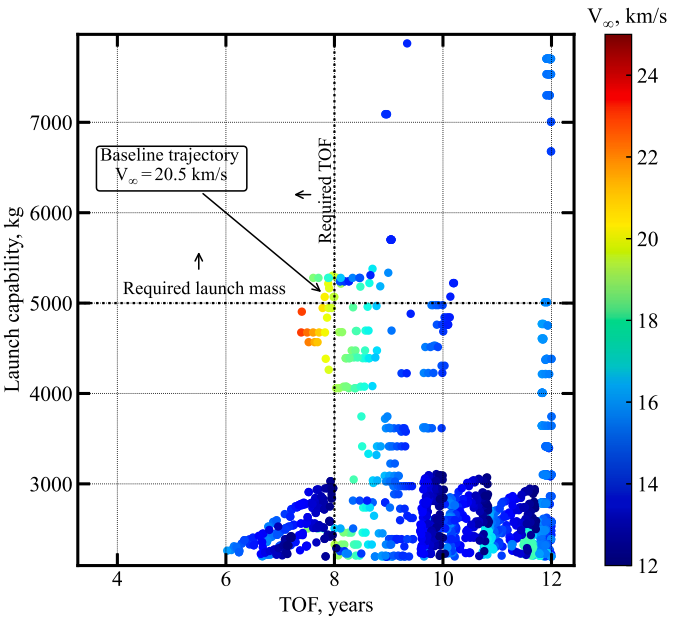

Fig. 5. Trajectory trade space showing time of flight (TOF), launch capability, and arrival V_∞. The top left quadrant indicates the region where the required launch mass constraint and the TOF constraint are satisfied. The baseline trajectory with V_∞ = 20.5 km/s is annotated.

Table 1
Aerocapture vehicle atmospheric entry state.

Parameter	Value
Entry altitude, km	1000
Entry longitude[a] , deg	−15.22
Entry latitude, deg	36.51
Atm. relative entry speed, km/s	29.36
Atm. relative heading angle[b], deg	85.78
Atm. relative EFPA, deg	−11.70

[a]Body-inertial frame following Hughes [33].
[b]Following the definition by Vinh [34].

level. The approach trajectory is completely defined by selection of two parameters: (1) the trajectory periapsis magnitude r_p, and (2) the angular position ψ on the ring created by the locus of periapses. Since the target orbit is polar, the angle ψ is chosen to be π which results in a 90 deg. inclination for the approach trajectory. The periapsis radius magnitude determines the entry flight-path angle (EFPA), and must be selected so that the EFPA falls within the aerocapture entry corridor. However, calculation of the corridor requires the vehicle state vector at atmospheric entry. Hence, an iterative approach is used to select $r_p = (25559 + 260)$ km which results in a planet-relative EFPA = −11.70 deg. and will be shown to fall within the aerocapture entry corridor in Section 5 and Fig. 9. Table 1 lists the nominal atmospheric entry conditions for the aerocapture vehicle. Fig. 6 shows the hyperbolic approach trajectory of the vehicle until atmospheric entry interface.

5. Aerocapture entry corridor and limiting trajectories

The atmospheric entry state vector (excluding the EFPA) defined in 1 is used to compute the aerocapture corridor for an MSL-derived aerocapture vehicle with L/D = 0.24, β = 146 kg/m^2, R_N = 1.125 m with a target capture orbit apoapsis altitude = 550,000 km. The aerocapture entry corridor is defined as the range of EFPA within which the entry vehicle must enter to accomplish aerocapture to the target orbit. If the vehicle enters too steep, then the vehicle will penetrate too deep into the atmosphere and may undershoot the target orbit or not exit the atmosphere altogether. If the vehicle enters too shallow,

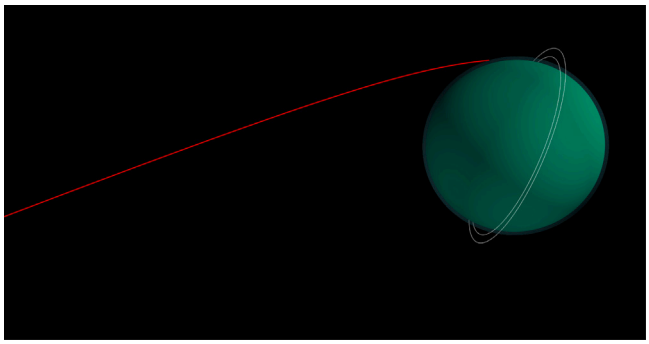

Fig. 6. Aerocapture vehicle hyperbolic approach trajectory till atmospheric entry interface.

Table 2
Aerocapture entry corridor and TCW.

Parameter	Value
Overshoot limit EFPA, deg.	−11.0088
Undershoot limit EFPA, deg.	−12.0264
TCW, deg	1.0176

the vehicle will exit the atmosphere without depleting enough energy and overshooting the target orbit or not getting captured at all. The undershoot limit is the steepest the vehicle can enter and using full lift-up the entire duration of the flight, is able to achieve the desired capture orbit target apoapsis. The overshoot limit is the shallowest the vehicle can enter and using full lift-down for the entire duration of the flight, is able to achieve the target apoapsis altitude post aerocapture. The aerocapture entry corridor is thus bounded by the undershoot (steep) and overshoot (shallow) EFPA limits and the width of the corridor is defined as the TCW. The undershoot and overshoot limits are computed by propagating entry trajectories for full lift-up and full lift-down trajectories starting with a guess lower and upper bound EFPA for each and using a bisection algorithm to solve for the limiting EFPA to achieve the desired target apoapsis altitude [31]. Table 2 shows the overshoot and undershoot limits (atmosphere-relative EFPA), and the TCW for a nominal density Uranus atmospheric profile. Fig. 7 shows the time evolution of altitude, deceleration load, peak heat rate and total heat load for the two limiting trajectories. The stagnation point heat rate calculations include both convective and radiative heating from empirical relations [24]. The convective heating rate $\dot{q}_c$ (in units of W/cm^2) is estimated using the Sutton–Graves empirical relation [35]:

$$\dot{q}_c = K \left(\frac{\rho_\infty}{R_N} \right)^{0.5} V^3 \tag{1}$$

where K = 0.6645E−8 for Uranus [36], ρ_∞ is the freestream atmospheric density in kilograms per cubic meter, R_N is the vehicle's effective nose radius in meters, and V is the freestream velocity in meters per second. The radiative heating rate $\dot{q}_r$ (in units of W/cm^2) is estimated using the following empirical correlation [37]:

$$\dot{q}_r = 8.125812 \times 10^{-3} \rho_\infty^{0.498140} \left(\frac{V}{10000} \right)^{15.113} \left(\frac{R_N}{0.291} \right) \tag{2}$$

The width of the entry corridor provides an upper bound for the acceptable EFPA error from approach navigation at entry interface. From Table 2, the TCW of approximately 1 deg. implies EFPA error exceeding ±0.5 deg.(3σ) would be unacceptable for aerocapture mission design. However, this is only an upper bound and the actual 3σ EFPA error must be smaller than ±0.5 deg. to account for atmospheric mean density variations as will be shown in Section 6.

The limiting trajectories provide considerable insight for the mission designer, as it provides nominal upper and lower bounds for the deceleration and heating environments during the early phase of the design.

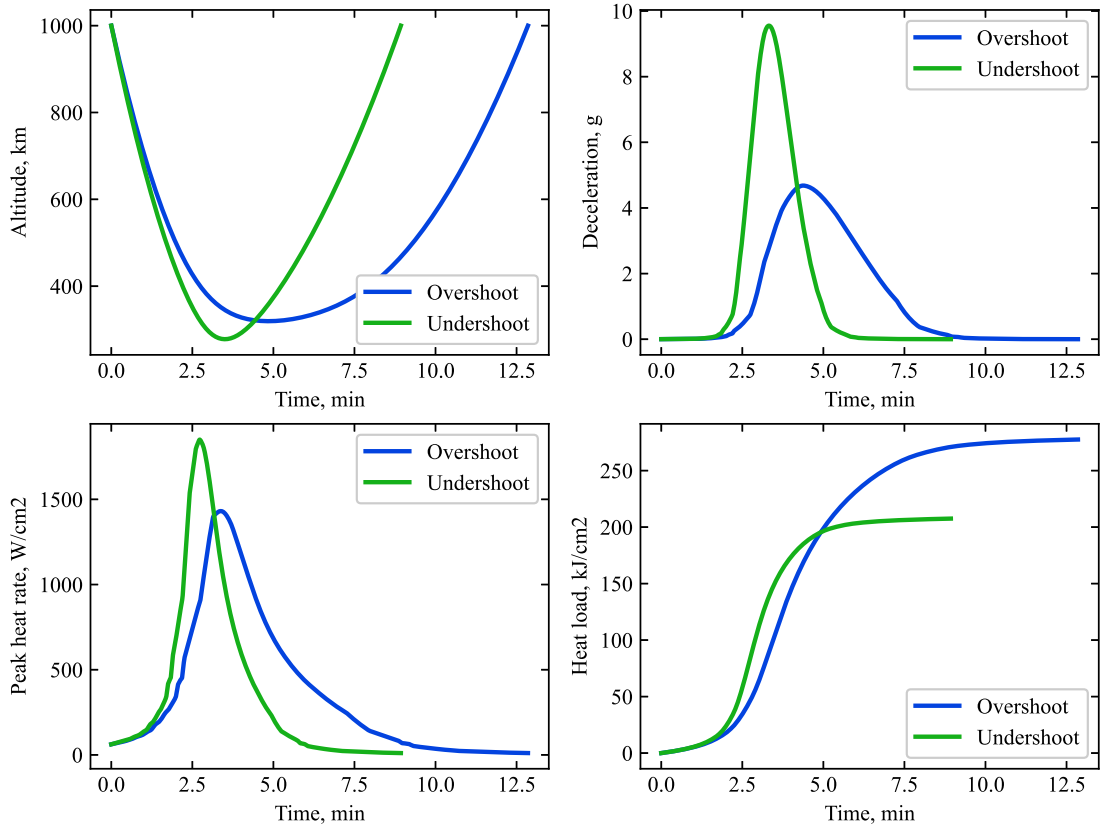

Fig. 7. Overshoot and undershoot trajectories for an MSL-derived aerocapture vehicle with L/D = 0.24, β = 146 kg/m^2, R_N = 1.125 m, target apoapsis altitude = 550,000 km.

Table 3
Effect of density variations on aerocapture corridor.

Parameter	Min. density	Nominal	Max. density
Overshoot limit EFPA, deg.	−11.3102	−11.1238	−10.9809
Undershoot limit EFPA, deg.	−12.3240	−12.1418	−12.0031
TCW, deg	1.0138	1.0180	1.0221

For example, the undershoot limit (steep entry) drives the maximum deceleration and peak heat rate values while the overshoot trajectory drives the total heat load value.

6. Effect of atmospheric uncertainties on target EFPA selection

The corridor bounds reported in Table 2 are for a nominal mean atmospheric profile from UranusGRAM. However, aerocapture mission analysis must also include the effect of atmospheric uncertainties as the corridor bounds are a function of the mean density profiles. The effect of these density variations must be accounted for when selecting the approach trajectory and the nominal target EFPA for the aerocapture entry system. Fig. 8 shows a representative sample of the minimum (−3σ), nominal, and maximum (+3σ) density profiles from UranusGRAM with random perturbations included. Table 3 shows the variation of the aerocapture corridor for the density profiles shown in Fig. 8.

Fig. 9 shows the effect of atmospheric density variations on the aerocapture entry corridor. The blue, green, and red boxes indicate the aerocapture corridor for the minimum, average, and maximum density atmospheric profiles shown in Fig. 8 respectively. There are three considerations to be accounted for when selecting the target EFPA: (1) The selected target EFPA (black dash-dot line) must pass through all of the blue, green, and red boxes. This ensures that if the vehicle enters at the target EFPA, the vehicle has enough control authority to achieve

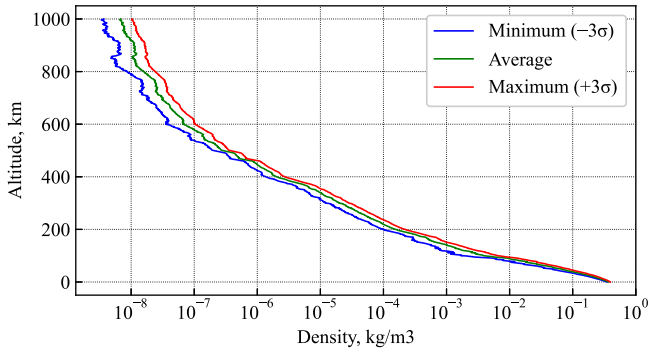

Fig. 8. A sample of minimum (−3σ), nominal, and maximum (+3σ) density profiles from UranusGRAM with random high frequency perturbations included. (For interpretation of the references to color in this figure legend, the reader is referred to the web version of this article.)

the desired exit conditions considering the full extent of mean density variations. (2) The +3σ EFPA value must fall within the overshoot limit for the minimum density atmosphere (blue solid line). This ensures that if the vehicle enters shallow (target EFPA + 3σ error) and the atmosphere density is minimum, there is still sufficient control authority to avoid the vehicle overshooting its target apoapsis, or in the worst case not getting captured. (3) The −3σ EFPA value must fall within the undershoot limit for the maximum density atmosphere (red solid line). This ensures that if the vehicle enters steep (target EFPA + −3σ error) and the atmosphere density is maximum, there is still sufficient control authority and the vehicle does not result undershooting its target orbit or in the worst case, getting trapped in the atmosphere. For the assumed delivery error (i.e. EFPA uncertainty), the above three constraints allow the vehicle to successfully accomplish aerocapture for any atmospheric

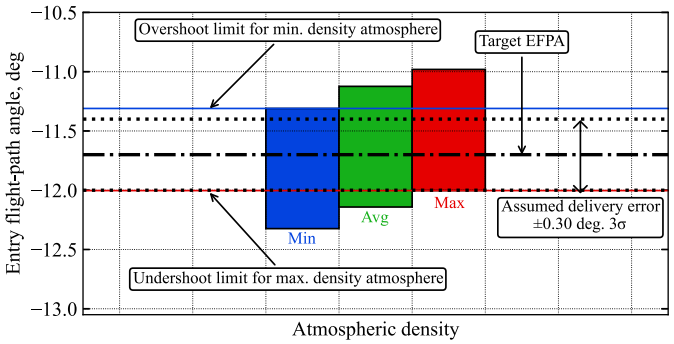

Fig. 9. Effect of density variations on corridor bounds. The black dash-dot line indicates the selected EFPA, and the black dotted lines indicate the assumed EFPA $\pm 3\sigma$ delivery error. (For interpretation of the references to color in this figure legend, the reader is referred to the web version of this article.)

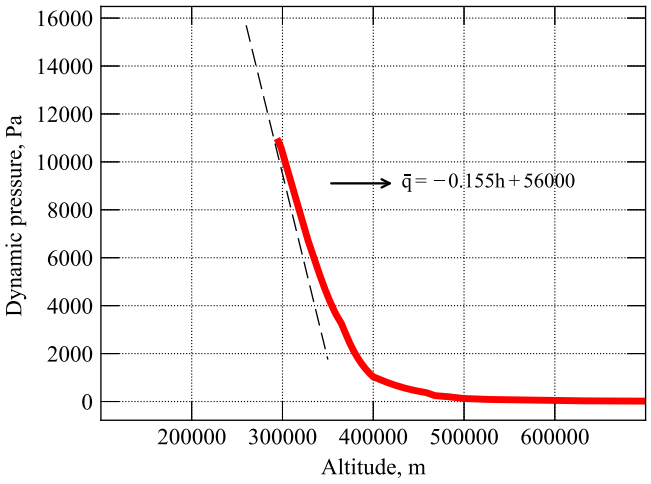

Fig. 10. Dynamic pressure profile during the entry of the aerocapture vehicle with $\beta = 146$ kg/m^2, $L/D = 0.24$ entering Uranus with full lift up. The solid red line indicates the dynamic pressure profile, and the dashed black line indicates the linear approximation below 350 km.

density profile within the minimum (-3σ) and the maximum ($+3\sigma$) limits from UranusGRAM. A navigation study to quantify the delivery errors from approach navigation is beyond the scope of this study and a value of ± 0.30 deg. (3σ) is assumed based on similar recent aerocapture mission studies [23,38].

The selected EFPA = −11.70 deg (planet-relative) satisfies the constraints listed above, and provides a small margin (0.1 deg.) against the overshoot boundary for the minimum density atmosphere. Simulations indicate that the combination of shallow EFPA and minimum density atmosphere makes the aerocapture vehicle prone to apoapsis overshoot and/or escape without getting captured, and a small margin is provided to safeguard against this undesirable scenario which will lead to certain loss of mission. The combination of steep EFPA and maximum density atmosphere only results in a modest apoapsis undershoot but never results in the vehicle getting trapped in the atmosphere.

7. Aerocapture guidance scheme

The aerocapture guidance algorithm guides the vehicle during atmospheric flight. This work uses bank angle modulation as the aerodynamic control method. Bank angle modulation has been successfully used on many planetary entry vehicles such as Apollo and the Mars Science Laboratory (MSL) and is considered a high-heritage flight control technique [39,40]. The lift vector is rotated around the velocity vector by banking the vehicle and the bank angle is the only control variable. The guidance scheme generates bank angle commands such that a set of terminal conditions are attained when the vehicle exits the atmosphere so as to achieve the desired apoapsis altitude. The guidance scheme used in the present work is a derivative of the guidance scheme developed by Cerimele and Gamble [41] and has been previously applied to aerocapture at Neptune [38]. The guidance scheme consists of two phases: (1) the equilibrium glide phase, and (2) the exit phase. During equilibrium glide, the vehicle attempts to maintain altitude acceleration $\ddot{h} = 0$. The bank angle command δ_{CMD} during the equilibrium glide phase is computed as [41]

$$\cos\delta_{CMD} = \cos\delta_{eq.\ gl.} - G_{\dot{h}}\dot{h} + G_{\bar{q}}\left(\frac{\bar{q}-\bar{q}_{ref}}{\bar{q}}\right) \tag{3}$$

where $\cos\delta_{eq.\ gl.}$ is the calculated equilibrium glide bank angle to which increments are added, and is given by [41]

$$\cos\delta_{eq.\ gl.} = \frac{mg}{C_L\bar{q}S}\left(1-\frac{v^2}{gr}\right) \tag{4}$$

where, m is the vehicle mass, g is the local gravitational acceleration, C_L is the vehicle lift coefficient, $\bar{q}$ is the dynamic pressure, S is the aerodynamic reference area, v is the atmosphere relative speed, and r is the radial distance from the center of the planet. The reference dynamic pressure $\bar{q}_{ref}$ is computed as [41]

$$\bar{q}_{ref} = -\frac{mg}{0.75C_LS}\left(1-\frac{v^2}{gr}\right) \tag{5}$$

The parameters $G_{\dot{h}}$ and $G_{\bar{q}}$ refer to the gain parameters and are chosen based on the method developed by Cerimele and Gamble [41]. The vehicle altitude dynamic response can be shown to be:

$$\ddot{h} + \frac{C_LS}{m}G_{\dot{h}}\dot{h} - \frac{C_LS}{m}G_{\bar{q}}\left(\bar{q}-\bar{q}_{ref}\right) = 0 \tag{6}$$

Eq. (6) can be approximated as a linear second order system by assuming $\bar{q} = ah + b$, and the system response is characterized by

$$\omega_n{}^2 = -\frac{C_LS}{m}G_{\bar{q}}a \tag{7}$$

$$2\zeta\omega_n = \frac{C_LS}{m}G_{\dot{h}} \tag{8}$$

For a vehicle with $\beta = 146$ kg/m^2, $L/D = 0.24$ entering Uranus with the entry state defined in Table 1 and using full lift up, the dynamic pressure as a function of altitude is shown in Fig. 10. A linear approximation can be made for the pressure profile as the vehicle descends below 350 km, where the aerodynamic forces become significant. Using $\omega_n = 0.05$ rad/s and $\zeta = 1.50$, the gain parameters can be calculated to be $G_h = 91.2$ and $G_{\bar{q}} = 9.81$.

During the descending leg of the aerocapture maneuver, the vehicle uses the accelerometer measurements to estimate the atmospheric density during the equilibrium glide phase until a predetermined altitude rate $\dot{h}$ is exceeded.

$$\rho_{est} = \frac{2\ ma_{drag}}{SC_Dv^2} \tag{9}$$

where, ρ_{est} is the estimated density, a_{drag} is the measured drag acceleration, and C_D is the drag coefficient. The present study assumes the drag deceleration can be accurately estimated from onboard accelerometer readings [42,43].

Once the predetermined altitude rate $\dot{h}$ threshold is exceeded, the density estimation is terminated and the guidance scheme starts predicting its apoapsis altitude at exit using full lift up for the remainder of the atmospheric flight. The prediction is done by numerically integrating the equations of motion using the density profile measured during the descending leg of the aerocapture maneuver. When the predicted apoapsis altitude at exit is sufficiently close to the desired value, the exit

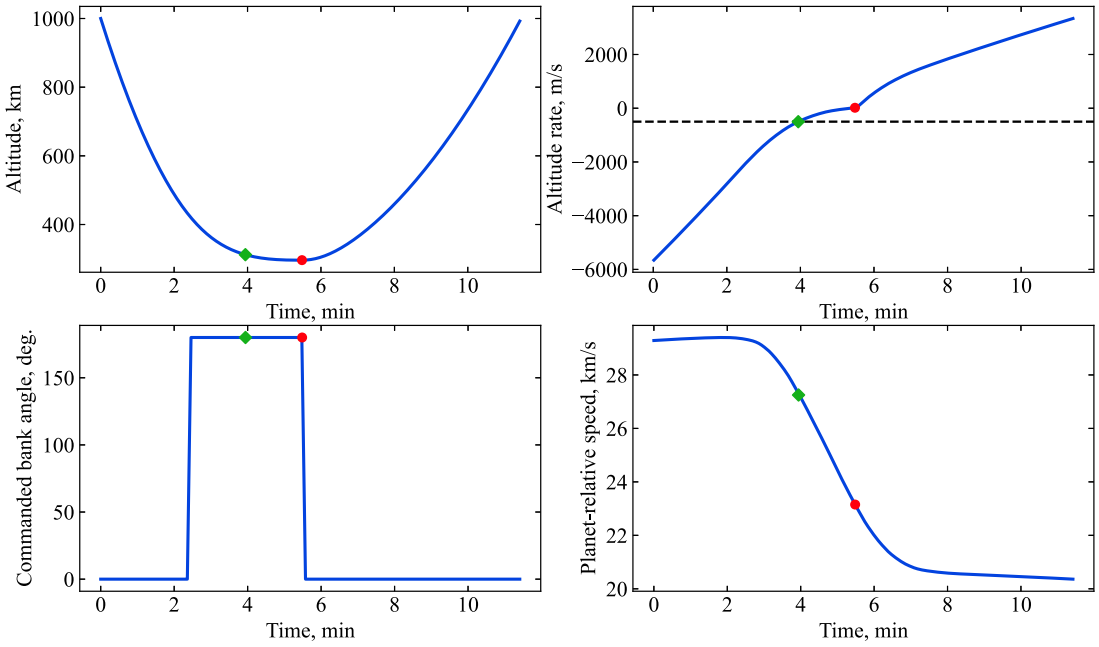

Fig. 11. Evolution of altitude, altitude rate, commanded bank angle, and planet-relative speed for a typical aerocapture entry trajectory near the shallow limit. The green diamond indicates the time where the altitude rate threshold is exceeded and where apoapsis prediction begins. The red circle indicates the time when exit phase guidance (full lift up) begins.

phase is initiated and the vehicle pulls out of the atmosphere with full lift up for the remainder of the atmospheric flight. The present study only considers apoapsis targeting and neglects out of plane motion and roll reversals for simplicity. Inclination errors from the atmospheric pass are expected to be small is not expected to significantly impact the results. A pseudo-controller is used to limit the maximum roll rate and acceleration to account for the time delay between bank angle command generation by the guidance scheme and actuation (eg: thruster firing) to achieve the commanded bank angle [44].

Fig. 11 shows the evolution of altitude, altitude rate, commanded bank angle, and planet-relative speed for a typical aerocapture entry trajectory near the shallow limit. Density measurement from accelerometer measurement starts at atmospheric entry and continues until a predefined altitude rate limit threshold (−500 m/s in this study) is exceeded, indicated by the green diamond. The red circle indicates the time when the guidance algorithm determines that full lift up for the remainder of the flight will yield the desired conditions to achieve the target apoapsis at atmospheric exit, and commands full lift up.

8. Performance analysis

Monte Carlo analysis is used to quantify the guidance scheme performance in the presence of combined navigation, atmospheric, and aerodynamic uncertainties. Nominal values of the parameters used and the associated uncertainties are listed in Table 4. For the approach navigation delivery uncertainties, only the uncertainty in the planet-relative EFPA is considered as this is the most important parameter of interest for aerocapture mission analysis. The relative uncertainty in other parameters such as the entry location, entry speed, and entry heading angle and the entry time are much less compared to that for the EFPA. The assumed $\pm 3\sigma$ uncertainty of 0.30 deg. is based on data available in the literature [23,38]. A dedicated navigation uncertainty to quantify the EFPA uncertainty is not within the scope of this study, and the assumed value is a believed to be reasonable approximation of the achievable EFPA error. The atmospheric mean density uncertainty ($\pm 3\sigma$) and random high-frequency perturbations are supplied by UranusGRAM [45]. For the aerodynamic uncertainty, a $\pm 3\sigma$ uncertainty of 0.04 is assumed (15% of the vehicle $L/D = 0.24$).

Table 4
Monte Carlo uncertainties.

Category	Variable	Nominal	Uncertainty	Distribution
Navigation	EFPA	−11.70 deg	±0.30 deg (3σ)	Normal
Atmosphere	Mean density	–	$\pm 3\sigma$ (GRAM)	Normal
	Random	–	rpscale = 1	Uniform
Aerodynamics	L/D	0.24	±0.04 (3σ)	Normal

The entry state used for the Monte Carlo simulations is defined in Table 1 with the EFPA distribution from Table 4. Vehicle parameters used are ballistic coefficient $\beta = 146$ kg/m^2, vehicle diameter = 4.5 m, and vehicle nose radius $R_N = 1.125$ m. The target apoapsis altitude is 550,000 km, and the apoapsis error tolerance used by the guidance algorithm is 10,000 km. The apoapsis prediction is initiated when the altitude rate exceeds −500 m/s and a guidance frequency of 2 Hz is used for the equilibrium glide phase. The maximum roll rate is constrained to 30 degrees per second. If the guidance algorithm detects the predicted apoapsis altitude at atmospheric exit is within the prescribed tolerance, the equilibrium glide phase is terminated and the exit phase is initiated.

For the Monte Carlo analysis, a set of 2000 trajectories is propagated with the navigation, atmospheric, and aerodynamic uncertainty distributions in Table 4. Of the 2000 trajectories, one trajectory (#1309) resulted in an unusually small capture orbit (apoapsis altitude = 149,053 km) and is considered a failure. Additional analysis revealed that this failure occurred due to a combination of shallow EFPA of −11.52 ($+1.8\sigma$) and low atmospheric density (-2.51σ) for which the guidance algorithm did not perform well. The orbit is so far off the target that it is not possible to correct the apoapsis to the desired 550,000 km within reasonable ΔV available to the spacecraft, and probe delivery also be difficult. The probability of this event occurring is approximately 1 in 1600, and is considered an outlier for this study and hence excluded from the results statistics. Fig. 12 shows the histogram of the apoapsis altitude and the apoapsis altitude and periapsis altitude from the Monte Carlo runs. Fig. 13 shows the scatter plots of the peak deceleration, peak stagnation-point heat rate, and the total heat load. Fig. 14 shows the histogram of the periapsis raise maneuver (PRM) ΔV to raise the

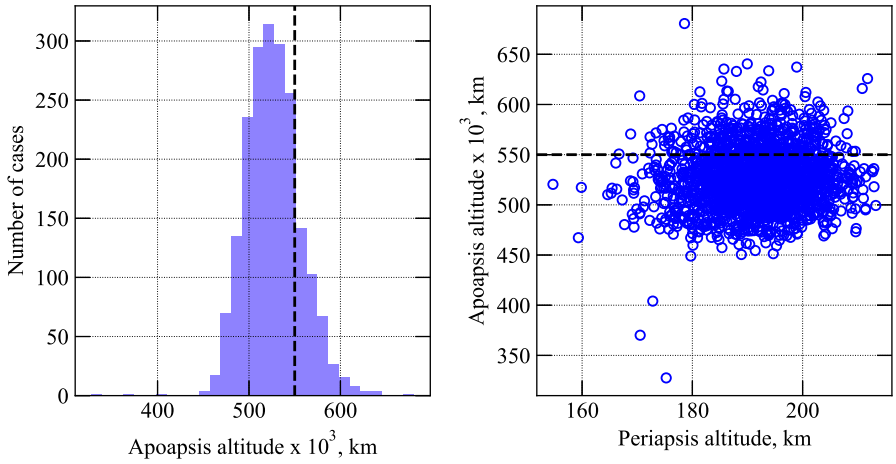

Fig. 12. Histogram of the apoapsis altitude (left) and the apoapsis altitude and periapsis altitude (right). The black dashed line indicates the target apoapsis altitude of 550,000 km.

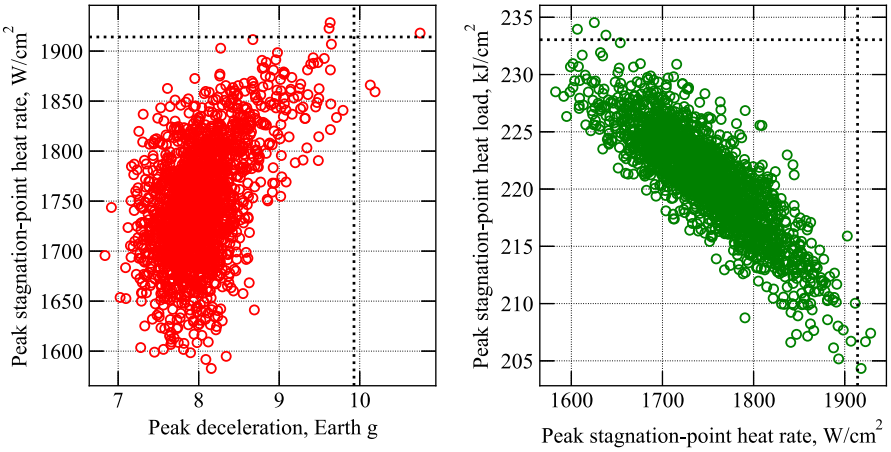

Fig. 13. Scatter plots of the peak deceleration, peak stagnation-point heat rate and the total heat load. The black dotted line indicates the 99.87-percentile values.

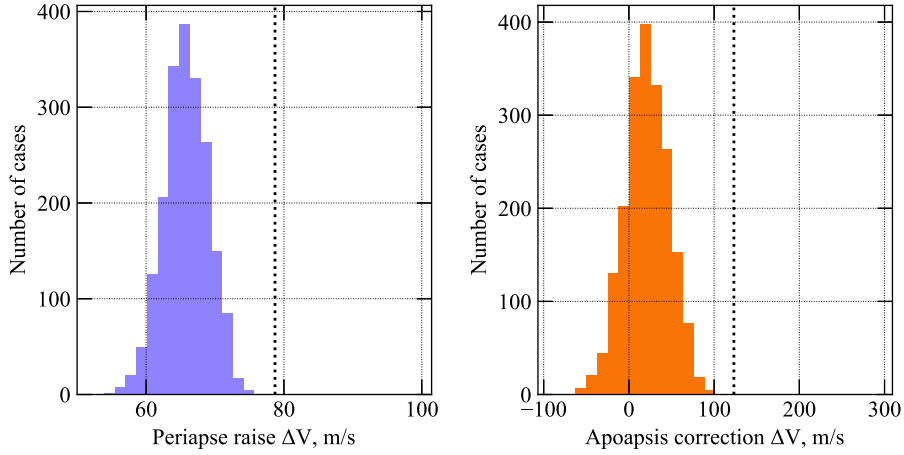

Fig. 14. Histogram of the periapsis raise maneuver ΔV (left), and histogram of the apoapsis raise maneuver ΔV. The black dotted line indicates the 99.87-percentile values.

periapsis outside the atmosphere, and the apoapsis correction ΔV to correct apoapsis targeting errors.

The apoapsis targeting accuracy is a key performance metric of the aerocapture mission concept. Accidental escape, target orbit overshoot or undershoot may require propulsive maneuvers to correct the errors and in some cases may lead to a partial or complete loss of mission. Table 5 shows some key statistical information for the achieved apoapsis altitudes at atmospheric exit.

Table 5
Statistics for initial post-aerocapture orbit apoapsis altitude.

Percentage captured	100%
Percentage within ±50,000 km of target	79.24%
Percentage within ±100,000 km of target	99.75%
Percentage within ±200,000 km of target	99.90%
Percentage outside ±200,000 km of target	0.10%

Table 6
Statistics from Monte Carlo simulations.

Parameter	Min.	0.13%-ile	Avg.	99.87%-ile	Max.
Apoapsis altitude, km	327,575	430,906	526,466	636,097	680,611
Periapsis altitude, km	155	163	192	213	213
Peak deceleration, g	6.84	7.06	8.01	9.93	10.75
Peak heat rate, W/cm^2	1583	1597	1747	1914	1928
Total heat load, kJ/cm^2	204	206	221	233	235
Periapsis raise ΔV, m/s	52.3	55.5	65.8	78.7	99.0
Apoapsis corr. ΔV, m/s	−87.8	−61.6	21.5	123.2	290.3

100% of the cases captured into orbit around Uranus, i.e. no cases resulted in an accidental escape which would lead to complete loss of mission. 79.24% of the cases achieved apoapsis within ±50,000 km of the target, and 99.75% of the cases achieved apoapsis within ±100,000 km of the target. These statistics indicate acceptable apoapsis accuracy. 0.10% of the cases (two cases) resulted in apoapsis outside ±200,000 km of the target, of which one case (#1309) mentioned earlier achieved apoapsis of 149,053 km and is considered a failure. The other case (#524) achieved an apoapsis of 327,574 km, and is considered a partial failure. These failures can be mitigated to some extent by better fine tuning of the guidance parameters, or by more advanced guidance schemes [46–48], but are not within the scope of the study. The primary objective of the performance analysis is to show that it is possible to achieve an initial post-aerocapture orbit having apoapsis reasonably close to the target (±100,000 km) with a very high confidence level (99.75% in this study). More trade studies to determine the optimal EFPA, decreasing the EFPA uncertainty through improvements in optical navigation, optimizing the guidance scheme parameters, increasing the vehicle L/D, and the use of advanced vehicle control techniques can reduce the apoapsis errors and hence lower the risk of failure.

Table 6 shows more statistics from the Monte Carlo simulation results. Note that these statistics do not include the one outlier case (#1309) which is considered a failure. The 99.87-percentile peak deceleration is 9.93 g, within the 12 g limit set in the study requirements. The 99.87-percentile peak stagnation-point heat rate is 1914 W/cm^2. This is within the tested limits of the HEEET TPS [49]. The 99.87-percentile total heat load is 233 kJ/cm^2, also within the limit set forth in the study requirements. Following atmospheric exit, the heat soaked aeroshell is jettisoned and the orbiter coasts to the first apoapsis where it performs a PRM to raise the periapsis outside the atmosphere to achieve the desired orbit periapsis altitude (4000 km). At the first periapsis passage, the orbiter performs another maneuver to correct the apoapsis error and achieve the initial capture orbit (4000 km × 550,000 km). Table 6 shows the statistics for the periapsis raise and the apoapsis correction maneuvers. The 99.87-percentile periapsis raise ΔV is 78.7 m/s and the 99.87-percentile apoapsis correction ΔV is 123.2 m/s. Note that in the case where the achieved apoapsis is slightly above the target value, the computed apoapsis correction ΔV is negative in Table 6. However, it is expected that in such a case of slight apoapsis overshoot, it may not be necessary to perform this maneuver and instead the mission plan can be modified to accommodate this slightly larger orbit. The larger orbit has the advantage of reducing the ΔV for probe targeting and orbiter deflection.

Table 7
Effect of delivery error (EFPA error) on capture rate and achieved apoapsis altitude targeting accuracy (measured from the target apoapsis altitude = 550e3 km).

Metric	3x higher (±0.90 deg 3σ)	Reference (±0.30 deg 3σ)	3x lower (±0.10 deg 3σ)
% captured	98%	100%	100%
% within ±50e3 km	63.50%	79.24%	78.50%
% within ±100e3 km	81.50%	99.75%	100%
% within ±200e3 km	83.50%	99.90%	100%
% outside ±200e3 km	14.50%	0.10%	0%

9. Sensitivity analysis

In this section, a parametric study is conducted to assess the sensitivity of aerocapture orbit insertion to accuracy of the entry trajectory, atmospheric mean density uncertainty, and the vehicle aerodynamic control authority compared to the reference values presented in Table 4. Finally, a guidance stress case is presented with a combination of high delivery error, high atmospheric mean density uncertainty, and reduced aerodynamic control authority.

9.1. Effect of delivery error (EFPA)

Two sets of Monte Carlo simulation are run: (1) one with 3x higher EFPA error (±0.90 deg. 3σ), and (2) one with 3x lower EFPA error (±0.10 deg 3σ) compared to the reference case presented in Table 4. The atmospheric and aerodynamic uncertainties are the same as listed in Table 4. 200 trajectories are propagated for each of the two cases. Table 7 compares the achieved orbit targeting accuracy from the two cases, along with the reference case. With the 3x higher EFPA error, 2% of the trajectories failed to capture in comparison to the reference case where no trajectories failed to capture. These cases are attributed to a combination of shallow EFPA and low density atmosphere against which the vehicle does not have sufficient control authority to achieve capture even with full lift down for the entire duration of the atmospheric flight. The orbit targeting accuracy is also reduced with only 81.50% achieving apoapsis within 100,000 km of the target compared to 99.75% for the reference case. Results for the case with 3x lower EFPA error does not show any improvement compared to the reference case. These results indicate that for the particular baseline vehicle design and interplanetary trajectory (L/D, V_∞) chosen in this study, the delivery error close to ±0.30 deg. is desirable and sufficient for acceptable aerocapture performance. The higher delivery error in this case increases the odds of not getting captured, and degrades orbit targeting accuracy.

Figs. 15 and 16 show the histogram of the apoapsis altitude and the apoapsis–periapsis scatter plot for the two cases. The cases which failed to capture are omitted from Fig. 15. Compared to the reference case (Fig. 12), several trajectories resulted in orbits much smaller than the target orbit. 14.50% of the cases resulted in orbits with apoapsis outside 200,000 km of the target (compared to 0.10% for the reference case). These orbits may not be practical for science objectives or continued mission operations are likely considered partial or complete failures in some cases. Fig. 16 shows the distribution for the case with the reduced EFPA error with 100% of the cases achieving apoapsis within 100,000 km of the target and has no outliers or not getting captured.

9.2. Effect of atmospheric mean density uncertainties

Two sets of Monte Carlo simulation are run: (1) one with 5x higher 3σ mean density uncertainty from UranusGRAM, and (2) one with 5x lower 3σ mean density uncertainty compared to the reference case presented in Table 4. The navigation and aerodynamic uncertainties are the same as listed in Table 4. Table 8 compares the achieved orbit accuracy from the two cases, along with the reference case. With the 5x higher mean density uncertainty, 5% of the trajectories failed to

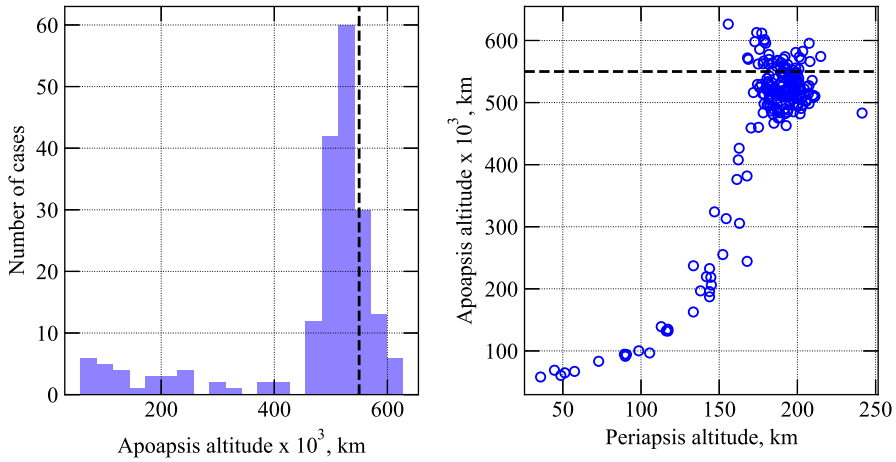

Fig. 15. Histogram of the apoapsis altitude (left) and the apoapsis altitude and periapsis altitude (right) for the case with 3x higher EFPA error (±0.90 deg. 3σ). The black dashed line indicates the target apoapsis altitude of 550,000 km.

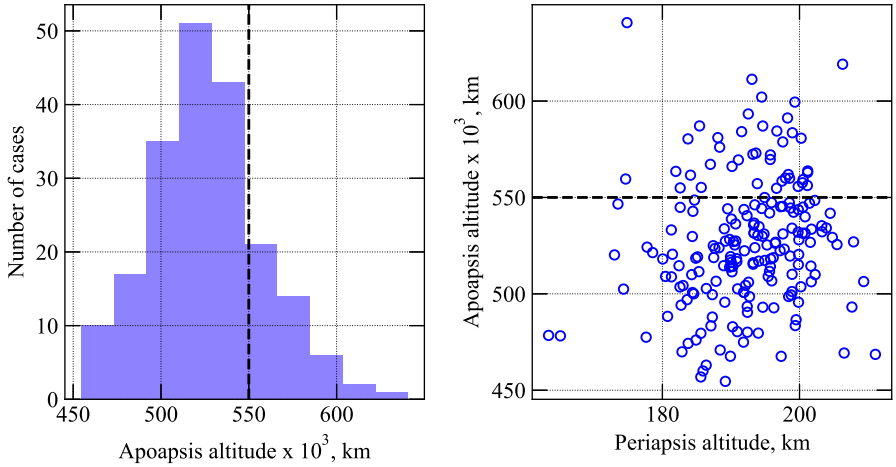

Fig. 16. Histogram of the apoapsis altitude (left) and the apoapsis altitude and periapsis altitude (right) for the case with 3x lower EFPA error (±0.10 deg. 3σ). The black dashed line indicates the target apoapsis altitude of 550,000 km.

capture in comparison to the reference case where no trajectories failed to capture. These cases are again attributed to a combination of shallow EFPA and low density atmosphere. The guidance scheme has some robustness against mean density variations, since it uses the measured density profile during the descending leg of aerocapture for apoapsis prediction. This could be attributed to why orbit targeting accuracy does not degrade substantially even with the significantly higher mean density uncertainty. 89% of the cases achieved within 200,000 km of the target, compared to 99.9% for the reference case. 6% of the cases resulted in orbits with apoapsis outside 200,000 km of the target (compared to 0.10% for the reference case) and are at least partial failures. The results for 5x lower mean density uncertainty do not show any improvement over the reference case. Figs. 17 and 18 show the histogram of the apoapsis altitude and the apoapsis–periapsis scatter plot for the two cases.

9.3. Effect of aerodynamic control authority (L/D)

The vehicle L/D is the key design parameter which determines how much aerodynamic control authority is available for the guidance scheme to control using bank angle modulation. The purpose of this section is to analyze the effect of changes in L/D on aerocapture performance, particularly if L/D is reduced. Two sets of Monte Carlo simulation are run: (1) one with 25% lower L/D (0.18), and (2) one with 25% higher L/D (0.30), compared to the reference case presented in Table 4. The navigation and atmospheric uncertainties are the same as listed in Table 4. Table 9 compares the orbit targeting accuracy from the two cases. No significant performance degradation or improvement is seen for both cases compared to the reference. As expected, the higher L/D slightly improves orbit accuracy compared to the reference, but it is not substantial.

Table 8
Effect of atmospheric mean density uncertainty on capture rate and achieved apoapsis altitude targeting accuracy (measured from the target apoapsis altitude = 550e3 km).

Metric	5x higher (5 × 3σ-GRAM)	Reference (3σ-GRAM)	5x lower (0.2 × 3σ-GRAM)
% captured	95%	100%	100%
% within ±50e3 km	70.5%	79.24%	79.00%
% within ±100e3 km	86.5%	99.90%	100%
% within ±200e3 km	89.0%	99.90%	100%
% outside ±200e3 km	6.0%	0.10%	0%

9.4. Stress case

A stress test for the guidance scheme is analyzed with 2x EFPA error (±0.20 deg. 3σ), 3x mean density uncertainty (3× 3σ-GRAM) compared to the reference uncertainties listed in Table 4, along with 20% lower vehicle L/D (L/D = 0.20). The purpose of the stress case is to evaluate how the guidance scheme responds to combined

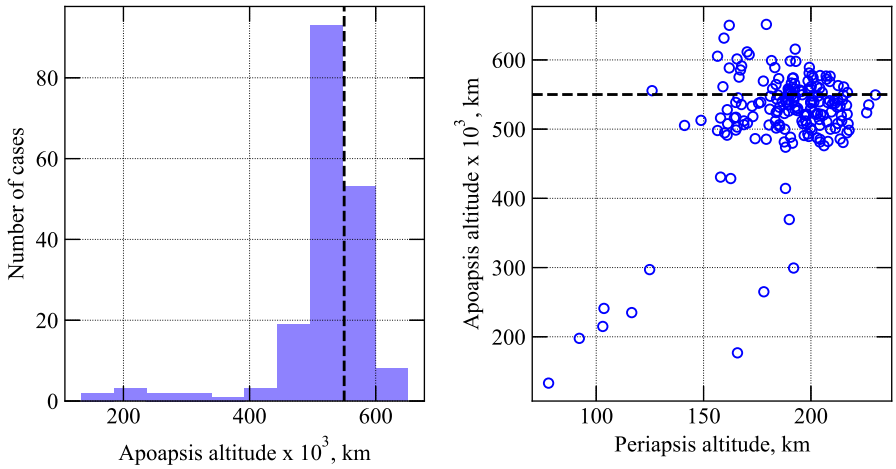

Fig. 17. Histogram of the apoapsis altitude (left) and the apoapsis altitude and periapsis altitude (right) for the case with 5x higher 3σ mean density uncertainty from UranusGRAM. The black dashed line indicates the target apoapsis altitude of 550,000 km.

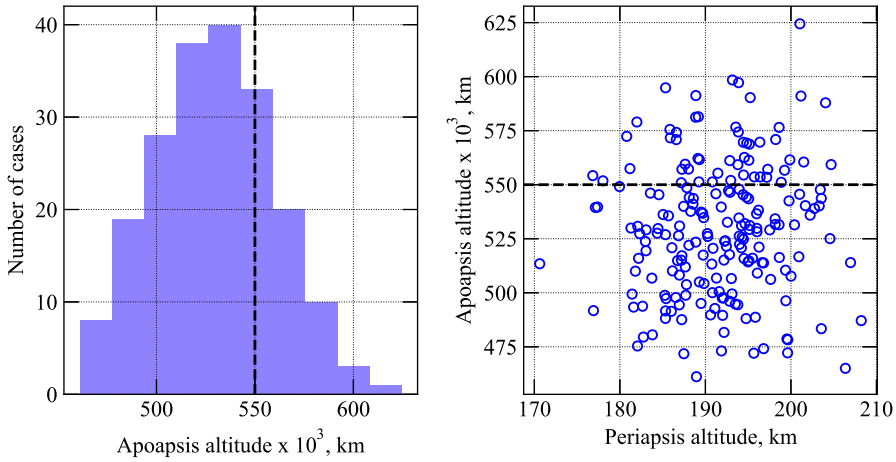

Fig. 18. Histogram of the apoapsis altitude (left) and the apoapsis altitude and periapsis altitude (right) for the case with 5x lower 3σ mean density uncertainty from UranusGRAM. The black dashed line indicates the target apoapsis altitude of 550,000 km.

Table 9
Effect of vehicle aerodynamic control authority (L/D) on capture rate and achieved apoapsis altitude targeting accuracy (measured from the target apoapsis altitude = 550e3 km).

Metric	25% lower ($L/D = 0.18$)	Reference ($L/D = 0.24$)	25% higher ($L/D = 0.30$)
% captured	100%	100%	100%
% within ±50e3 km	78%	79.24%	84%
% within ±100e3 km	99.5%	99.90%	100%
% within ±200e3 km	100%	99.90%	100%
% outside ±200e3 km	0%	0.10%	0%

Table 10
Combined effect of 2x EFPA error, 3x mean density uncertainty, and 20% lower L/D on capture rate and achieved apoapsis altitude targeting accuracy.

Metric	Stress case	Reference
% captured	98.5%	100%
% within ±50e3 km	74%	79.24%
% within ±100e3 km	90.5%	99.90%
% within ±200e3 km	94%	99.90%
% outside ±200e3 km	4.5%	0.10%

higher than expected navigation and atmospheric uncertainties and also reduced aerodynamic control authority. Table 10 compares the achieved orbit accuracy from the stress case, along with the reference case for comparison. 98.5% of the cases achieved orbit insertion. Orbit targeting accuracy is slightly degraded compared to the reference case, but is still satisfactory. Table 11 lists the statistics from Monte Carlo simulations for the stress case. 4.5% of the cases resulted in orbits outside 200,000 km of the target and may be considered failures. The results indicate that the guidance algorithm is robust enough to be able to accommodate these higher than expected uncertainties. Compared to the reference case which had total failure rate of 0.10%, (defined as the sum of cases not captured and those with apoapsis outside 200,000 km), the stress case has a failure rate of only 6% which is still reasonable considering the significant increase in both navigation (2x) and atmospheric (3x) uncertainties and reduction in L/D (80%).

10. Probe delivery

There are two options for probe delivery: (1) deliver the probe from the hyperbolic approach trajectory before orbit insertion, and (2) deliver the probe from orbit after orbit insertion. In the first approach, the orbiter releases the probe during hyperbolic approach, and then performs an orbiter-divert and timing burn. The orbiter arrives overhead immediately after the probe entry to relay data from the probe. Immediately after the probe mission is complete, the orbiter performs orbit insertion. In the second approach, the probe is carried through orbit insertion and then released from orbit. At or near the apoapsis, the orbiter performs a probe targeting maneuver (PTM) to allow the orbit

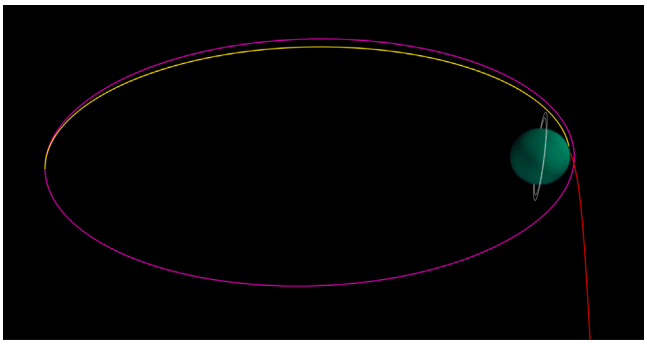

Fig. 19. Hyperbolic approach trajectory (red), coast phase after aerocapture maneuver (yellow), and initial capture orbit after periapsis raise maneuver at apoapsis (magenta). (For interpretation of the references to color in this figure legend, the reader is referred to the web version of this article.)

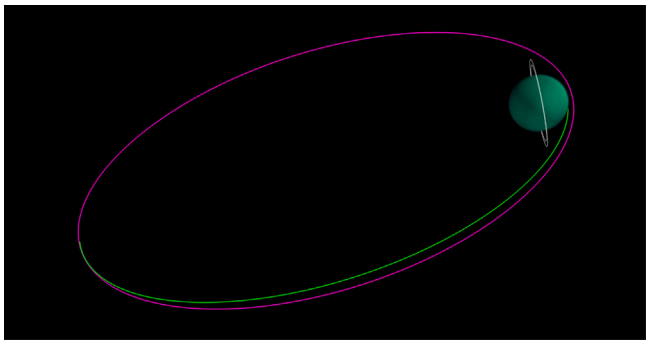

Fig. 20. Probe approach trajectory (green) following the probe targeting maneuver, and the orbiter trajectory (magenta) following the orbiter deflection maneuver. (For interpretation of the references to color in this figure legend, the reader is referred to the web version of this article.)

periapsis to dip inside the atmosphere and the probe is released on this trajectory. The orbiter then performs an orbiter deflection and timing burn to return to its initial orbit prior to the PTM, and will fly over the entry zone during the probe descent to relay data. Historically mission concept studies tend to prefer the first approach for outer planet missions using propulsive capture [12], as releasing the probe prior to orbit insertion offers two advantages: (1) the orbiter-divert maneuver ΔV for this approach is very small (typically 10–20 m/s), and (2) since the ΔV for propulsive insertion is generally large, not having to carry the probe through orbit insertion reduces the propellant required for the orbit insertion burn. However, this approach also comes with some disadvantages: (1) Releasing the probe during approach implies there is very little flexibility in choosing the entry location. (2) This approach poses operational challenges as the probe entry is immediately followed by orbit insertion both of which are mission critical events occurring within a span of a few hours. (3) The coast time is generally 50+days after probe release, and there is no possibility of adjusting the probe trajectory once released. It is possible the probe enters a storm system or a dry spot which may have developed during the coast phase and lead to diminished science return. This was the case with the Galileo probe which entered a dry spot in Jupiter's atmosphere and resulted in it not being able to obtain some key measurements such as the water vapor abundance [50].

In the second option with probe delivery after orbit insertion, the orbit insertion and probe entry events are decoupled and the probe entry can be accomplished during any orbit. This approach has several advantages: (1) Decoupling the orbit insertion and probe delivery implies the two mission critical events are not closely spaced in time. (2) There is more flexibility in the choice of the entry location and entry time, and ample backup opportunities for probe deployment. In addition, there is the opportunity for the orbiter to perform close up reconnaissance of the planned entry location prior to selecting a site and releasing the probe. (3) Entry from orbit results in significantly lower entry speeds compared to entry from hyperbolic approach, and this implies the probe can be designed to withstand a less severe aerothermal environment. The disadvantages of the second approach are: (1) for propulsive insertion, carrying the probe through orbit insertion requires more propellant for the orbit insertion burn. (2) the probe targeting and orbiter deflection maneuvers can be large if the orbit is not highly elliptical. The second approach is currently the preferred method [9], and is selected as the baseline probe delivery method for this study. Fig. 19 shows the hyperbolic approach trajectory, post-aerocapture coast to apoapsis, and the initial orbit from which the entry probe is delivered.

The orbiter performs a probe targeting maneuver near the orbit apoapsis. This maneuver dips the orbit periapsis inside the atmosphere, so as to achieve a desired negative EFPA at the probe entry interface.

Table 11
Statistics from Monte Carlo simulations for the stress case with increased navigation and atmospheric uncertainty, along with reduced vehicle L/D.

Parameter	Min.	0.13%-ile	Avg.	99.87%-ile	Max.
Apoapsis altitude, km	38,937	67,269	511,164	664,592	683,243
Periapsis altitude, km	0	31	185	222	223
Peak deceleration, g	6.27	6.33	8.19	13.51	14.46
Peak heat rate, W/cm^2	1503	1512	1749	2020	2036
Total heat load, kJ/cm^2	203	203	221	245	246
Periapsis raise ΔV, m/s	52.1	53.6	70.45	324.51	373.38
Apoapsis corr. ΔV, m/s	−89.27	−77.92	60.65	2424	2914

Table 12
Probe atmospheric entry state.

Parameter	Value
Entry altitude, km	1000
Entry longitude[a] , deg	−10.96
Entry latitude, deg	67.49
Atm. relative entry speed, km/s	20.4018
Atm. relative heading angle[b], deg	87.19
Atm. relative EFPA, deg	−14.03

[a]Body-inertial frame following Hughes [33].
[b]Following the definition by Vinh [34].

The selection of the target EFPA must incorporate the following considerations: (1) The EFPA must not be too shallow, or else the probe will skip out of the atmosphere. (2) The EFPA must not be too steep that the probe will be subject to excessive deceleration or peak stagnation-point heat rate. (3) The total heat load during entry must be within an acceptable level to limit the TPS mass fraction. (4) The PTM maneuver ΔV must not exceed 100 m/s (value arbitrarily selected for this study). Following the PTM, the orbiter releases the probe which then coasts to the atmospheric interface where it begins its entry sequence. The orbiter then performs an orbiter-deflection maneuver (ODM) so that the orbiter periapsis is raised outside the atmosphere back to its initial orbit prior to the PTM as shown in Fig. 20. A detailed flight system design for the probe and selection of the PTM and ODM location and maneuver ΔV is not performed in this study. Instead, one feasible solution is selected and used to compute the key entry system design parameters such as peak deceleration, peak heat rate and total heat load.

For this study, the PTM is performed just before apoapsis at true anomaly $\theta^* = 178$ deg. A propulsive maneuver with $\Delta V = 90$ m/s is applied in the direction opposite to the orbital velocity which dips the orbit periapsis to −716 km and results in a planet-relative EFPA = −14 deg. for the probe trajectory. The probe atmospheric entry state is shown in Table 12. Note the atmospheric entry speed for probe delivery from orbit is approximately 20 km/s compared to about 29 km/s for delivery from a hyperbolic approach trajectory.

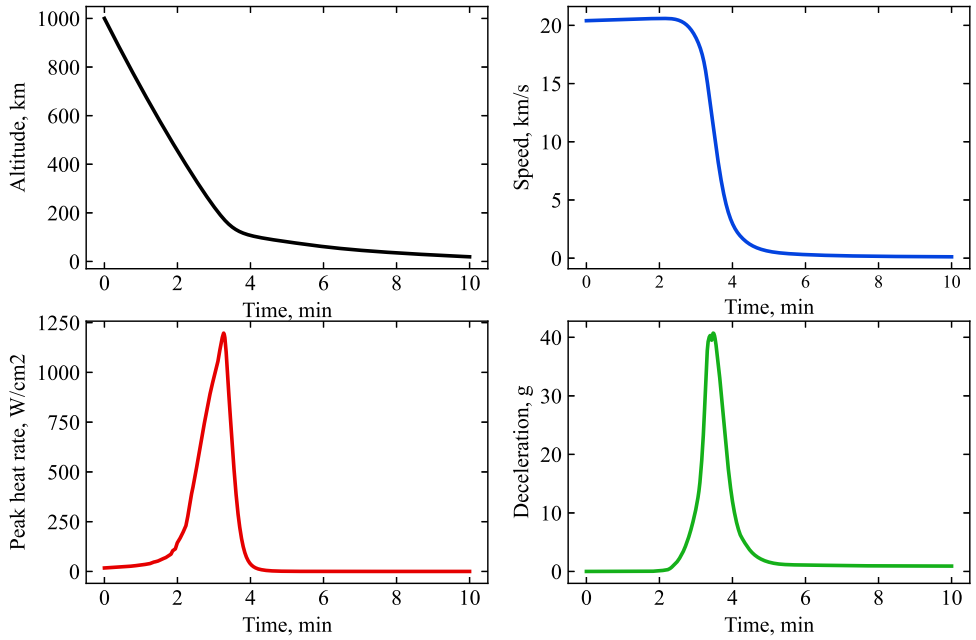

Fig. 21. Probe entry trajectory showing the time history of altitude, speed, sensed deceleration, and stagnation-point heat rate. The entry speed at atmospheric interface is approximately 20 km/s. The peak heat-rate and deceleration is 1240 W/cm^2 and 40 g respectively.

Following the PTM and probe release immediately after, the ODM is performed approximately 9 h later at $\theta^* = 182$ deg. A propulsive maneuver with $\Delta V = 90$ m/s is applied in the direction of the orbital velocity to raise the orbit periapsis outside the atmosphere and back to 4000 km. Detailed flight system design of the probe such as the entry system and descent module design is not performed. This study uses the probe design parameters from the UOP Flagship mission study: mass = 300 kg, vehicle diameter = 1.26 m, and nose radius = 0.40 m. Fig. 21 shows the time history of altitude, speed, sensed deceleration, and stagnation-point heat rate for entry probe trajectory. The peak stagnation-point heat rate is 1240 W/cm^2. The peak deceleration is 40 g, and the total heat load is 60 kJ/cm^2. The orbiter flies above the entry probe during its descent after entry and relays the data back to Earth.

11. Flight system mass and ΔV summary

Table 13 shows the high-level flight system mass budget and ΔV summary from launch till the start of the orbital phase of the mission. The initial mass m_0 refers to the mass of the flight system at the start of the event, and the final mass m_f refers to the system mass at the end of the event which is calculated using the rocket equation as follows

$$m_f = m_0 \exp\left(-\frac{\Delta V}{I_{sp} g_0}\right) \tag{10}$$

where I_{sp} is the propulsion system specific impulse (assumed 320 s) and $g_0 = 9.80665$ m/s^2 is the standard gravitational acceleration on the Earth's surface. Just prior to the aerocapture maneuver, the 400 kg MSL-derived cruise stage is jettisoned. Immediately after aerocapture, the aeroshell structure and the heat-soaked TPS are jettisoned. The mass fraction of the aeroshell structure is assumed to 0.20 based on the MSL entry system, and the TPS mass fraction is conservatively assumed to be 0.20 for the 233 kJ/cm^2 total heat load.

Following orbit insertion and probe delivery, the orbital phase of the mission starts with a wet mass of 1429 kg. The nominal duration of the orbital phase is 10 years, based the same total mission life of 18 years used by the UOP Flagship mission study [9]. It is noted that the 10-year mission life is double that of the current baseline UOP mission. The design of the orbital phase and the subsequent moon tour is outside the scope of this study. At the end of the orbital tour, a small propulsive burn (estimated to be less than 50 m/s) will be used to send the spacecraft into the Uranus atmosphere for disposal.

Table 13
Flight system mass and ΔV summary.

Event	m_0, kg	ΔV, m/s	ΔM, kg	m_f, kg
Launch capability	5069	–	–	5069
Deep space maneuver	5069	1040	−1430	3639
Cruise stage jettison	3639	–	−400[a]	3239
Aeroshell and TPS jettison	3238	–	−1295[b,c]	1943
Periapsis raise maneuver	1943	79	−48	1895
Apoapsis correction maneuver	1895	123	−73	1822
Probe targeting maneuver	1822	90	−51	1771
Probe release	1771	–	−300	1471
Orbiter deflection	1471	90	−42	1429

[a]Based on an MSL-derived cruise stage.
[b]Based on an MSL-derived structural mass fraction = 0.2.
[c]Based on a conservative TPS mass fraction = 0.20 for the computed 99.87-percentile 233 kJ/cm^2 total heat load from the work by Venkatapathy et al. [49].

12. Conclusions

The study presented a Flagship-class Uranus orbiter and probe mission concept using aerocapture. The aerocapture feasibility chart, a graphical method for conceptual aerocapture mission design is used to select a baseline aeroshell design and set constraints on the arrival V_∞. A 7.8-year baseline interplanetary trajectory with a launch mass capability of 5069 kg on the Falcon Heavy Expendable launch vehicle is selected. The aerocapture vehicle design uses an MSL-derived aeroshell with $L/D = 0.24$ and HEEET thermal protection system, and is shown to provide acceptable control authority for aerocapture. Monte Carlo simulation is used to analyze the effect of navigation, atmospheric, and aerodynamic uncertainties on aerocapture system performance and is shown to provide satisfactory orbit targeting accuracy post aerocapture. The probe targeting and orbiter deflection maneuvers to deliver a 300-kg atmospheric probe from orbit is computed. The mission concept delivers an orbiter with a wet mass of 1429 kg at the start of the orbital phase of the mission. With a nominal orbital mission life of 10 years which is double that of the current baseline UOP mission the

proposed mission concept allows the orbiter to perform more extensive moon tours and also follow up observations of interesting scientific discoveries. While a cost estimate was not done, the mission uses a cost-effective launcher and an MSL-derived entry system with extensive flight heritage and is expected to fit within the budgetary constraints of a Flagship mission.

Declaration of competing interest

The authors declare that they have no known competing financial interests or personal relationships that could have appeared to influence the work reported in this paper.

Data availability

Jupyter Notebooks to reproduce the study results are available at the AMAT website https://amat.readthedocs.io/en/master/acta-astronautica.html#uranus-orbiter-and-probe

Acknowledgments

The author acknowledges Anastassios Petropoulos at the NASA Jet Propulsion Laboratory, and Nitin Arora formerly at the NASA Jet Propulsion Laboratory for generating the interplanetary trajectory dataset originally created for the Ice Giants Pre-Decadal mission study and is used for this study.

References

[1] C.S. Arridge, N. Achilleos, J. Agarwal, C. Agnor, R. Ambrosi, N. André, S.V. Badman, K. Baines, D. Banfield, M. Barthélémy, et al., The science case for an orbital mission to Uranus: Exploring the origins and evolution of ice giant planets, Planet. Space Sci. 104 (2014) 122–140, http://dx.doi.org/10.1016/j.pss.2014.08.009.

[2] O. Mousis, D.H. Atkinson, T. Cavalié, L. Fletcher, M. Amato, S. Aslam, F. Ferri, J.-B. Renard, T. Spilker, E. Venkatapathy, et al., Scientific rationale for uranus and neptune in situ explorations, Planet. Space Sci. 155 (2018) 12–40, http://dx.doi.org/10.1016/j.pss.2017.10.005.

[3] S.K. Atreya, M.D. Hofstadter, K.R. Reh, J.H. In, Icy giant planet exploration: are entry probes essential? Acta Astronaut. 162 (2019) 266–274, http://dx.doi.org/10.1016/j.actaastro.2019.06.020.

[4] Engineering, and Medicine National Academies of Sciences, Vision and Voyages for Planetary Science in the Decade 2013–2022, National Academies Press, Washington D.C., 2011, Ch. 7.

[5] Engineering, and Medicine National Academies of Sciences, Origins, Worlds, and Life: A Decadal Strategy for Planetary Science and Astrobiology 2023–2032, National Academies Press, Washington D.C., 2022, http://dx.doi.org/10.17226/26522, Ch. 22.

[6] S. Jarmak, E. Leonard, A. Akins, E. Dahl, D. Cremons, S. Cofield, A. Curtis, C. Dong, E. Dunham, B. Journaux, et al., QUEST: A new frontiers uranus orbiter mission concept study, Acta Astronaut. 170 (2020) 6–26, http://dx.doi.org/10.1016/j.actaastro.2020.01.030.

[7] L. Fletcher, A. Simon, M. Hofstadter, C. Arridge, I.J. Cohen, A. Masters, K. Mandt, A. Coustenis, Ice giant system exploration in the 2020s: an introduction, Phil. Trans. R. Soc. A 378 (2187) (2020) 20190473, http://dx.doi.org/10.1098/rsta.2019.0473.

[8] B. Bairstow, Y.H. Lee, K. Oxnevad, Mission analysis for next-generation RTG study, in: 2018 IEEE Aerospace Conference, IEEE, Big Sky, MT, 2018, pp. 1–19, http://dx.doi.org/10.1109/AERO.2018.8396411.

[9] A. Simon, F. Nimmo, R.C. Anderson, et al., Uranus Orbiter and Probe, Planetary Mission Concept Study for the 2023–2032 Decadal Survey, National Aeronautics and Space Administration, 2021, URL https://tinyurl.com/2p88fx4f.

[10] A. Austin, G. Afonso, et al., Enabling and enhancing science exploration across the solar system: Aerocapture technology for SmallSat to flagship missions, Bull. Amer. Astron. Soc. 54 (4) (2021) http://dx.doi.org/10.3847/25c2cfeb.4b23741d.

[11] S. Dutta, M. Perez-Ayucar, A. Fedele, R. Gardi, G.D. Calabuig, S. Schuster, J.-P. Lebreton, H.K. Ali, K. Sayanagi, I. Sakraker Ozmen, et al., Aerocapture as an enhancing option for ice giants missions, Bull. Amer. Astron. Soc. 53 (4) (2021) 046, http://dx.doi.org/10.3847/25c2cfeb.e8e49d0e.

[12] M.D. Hofstadter, A. Simon, K. Reh, J. Elliot, Ice Giants Pre-Decadal Study Final Report, Tech. Rep. JPL D-100520, NASA, Pasadena, CA, 2017, pp. 473–488, URL https://www.lpi.usra.edu/icegiants/mission_study/.

[13] General Electric Co., Generic Aerocapture Atmospheric Entry Study, Volume 1, Tech. Rep. NASA-CR-164161, Philadelphia, PA, 1980, URL https://ntrs.nasa.gov/api/citations/19810012569/downloads/19810012569.pdf.

[14] D.E. Florence, Aerothermodynamic design feasibility of a generic planetary aerocapture/aeromaneuver vehicle, Thermophys. Atmosph. Entry (1982) 477–519, http://dx.doi.org/10.2514/5.9781600865565.0477.0519.

[15] S. Hoffman, A comparison of aerobraking and aerocapture vehicles for interplanetary missions, in: Astrodynamics Conference, Seattle, WA, 1984, p. 2057, http://dx.doi.org/10.2514/6.1984-2057.

[16] J.L. Hall, M.A. Noca, R.W. Bailey, Cost-benefit analysis of the aerocapture mission set, J. Spacecr. Rockets 42 (2) (2005) 309–320, http://dx.doi.org/10.2514/1.4118.

[17] P. Agrawal, G.A. Allen, E.B. Sklyanskiy, H.H. Hwang, L.C. Huynh, K. McGuire, M.S. Marley, J.A. Garcia, J.F. Aliaga, R.W. Moses, Atmospheric entry studies for uranus, in: 2014 IEEE Aerospace Conference, IEEE, Big Sky, MT, 2014, pp. 1–19, http://dx.doi.org/10.1109/AERO.2014.6836417.

[18] T.R. Spilker, M. Adler, N. Arora, P.M. Beauchamp, J.A. Cutts, M.M. Munk, R.W. Powell, R.D. Braun, P.F. Wercinski, Qualitative assessment of aerocapture and applications to future missions, J. Spacecr. Rockets 56 (2) (2018) 536–545, http://dx.doi.org/10.2514/1.A34056.

[19] S.J. Saikia, J. Millane, Y. Lu, A. Mudek, A. Arora, P. Witsberge, K. Hughes, J.M. Longuski, T. Spilker, A. Petropoulos, N. Arora, J. Cutts, J. Elliott, J. Sims, K. Reh, Aerocapture assessment for NASA ice giants pre-decadal survey mission study, J. Spacecr. Rockets 58 (2) (2021) 1–11, http://dx.doi.org/10.2514/1.A34703.

[20] A.P. Girija, S.J. Saikia, J.M. Longuski, J.A. Cutts, A unified framework for aerocapture systems analysis, in: 2019 AAS/AIAA Astrodynamics Specialist Conference, no. AAS 19-811, Portland, ME, URL https://engrxiv.org/xtacw/.

[21] A.P. Girija, S.J. Saikia, J.M. Longuski, S. Bhaskaran, M.S. Smith, J.A. Cutts, Aerocapture performance analysis for a neptune mission using a heritage blunt-body aeroshell , in: 2019 AAS/AIAA Astrodynamics Specialist Conference, no. AAS 19-815, Portland, ME, URL https://engrxiv.org/preprint/view/668.

[22] J. Hofgartner, M. Hofstaeder, S. Smrekar, J. Hall, J. Brophy, A. Chmielewski, B. Frazier, J. Elliot, A. Austin, J. Cutts, et al., Innovative Flagship Mission Concept Studies: Uranus-Tempest, Enceladus-Ark, Venus-Dynamo, Tech. Rep. CL#20-2269, Jet Propulsion Laboratory, 2019, URL https://trs.jpl.nasa.gov/bitstream/handle/2014/53000/CL%2320-2269.pdf.

[23] D.P. Lubey, S. Bhaskaran, N. Bradley, Z. Olikara, Ice giant exploration via autonomous optical navigation, in: 2020 AAS/AIAA Astrodynamics Specialist Conference, AAS, South lake Tahoe, CA, 2020, URL https://trs.jpl.nasa.gov/bitstream/handle/2014/53199/CL%2320-3375.pdf.

[24] A.P. Girija, S.J. Saikia, J.M. Longuski, Y. Lu, J.A. Cutts, Quantitative assessment of aerocapture and applications to future solar system exploration, J. Spacecr. Rockets 59 (4) (2022) 1074–1095, http://dx.doi.org/10.2514/1.A35214.

[25] A. Duvall, C. Justus, V. Keller, Global reference atmospheric model (GRAM) series for aeroassist applications, in: 43rd AIAA Aerospace Sciences Meeting and Exhibit, no. January 2005, AIAA, Reno, NV, 2005, http://dx.doi.org/10.2514/6.2005-1239.

[26] H.L. Justh, A. Dwyer Cianciolo, Global reference atmospheric model (GRAM) upgrades and new releases, in: 43rd COSPAR Scientific Assembly, Sydney, Australia, 2021, URL https://ui.adsabs.harvard.edu/abs/2021cosp...43E.752J/abstract.

[27] J. Mansell, N. Kolencherry, K. Hughes, A. Arora, H. Chye, K. Coleman, J. Elliott, S. Fulton, N. Hobar, B. Libben, Y. Lu, J. Millane, A. Mudek, L. Podesta, J. Pouplin, E. Shibata, G. Smith, B. Tackett, T. Ukai, P. Witsberger, S. Saikia, Oceanus: A multi-spacecraft flagship mission concept to explore saturn and uranus, Adv. Space Res. 59 (9) (2017) 2407–2433, http://dx.doi.org/10.1016/j.asr.2017.02.012.

[28] M. Hofstadter, A. Simon, S. Atreya, D. Banfield, J.J. Fortney, A. Hayes, M. Hedman, G. Hospodarsky, K. Mandt, A. Masters, et al., Uranus and neptune missions: A study in advance of the next planetary science decadal survey, Planet. Space Sci. 177 (2019) 104680, http://dx.doi.org/10.1016/j.pss.2019.06.004.

[29] I. Cohen, C. Beddingfield, R. Chancia, G. DiBraccio, M. Hedman, S. MacKenzie, B. Mauk, K. Sayanagi, K. Soderlund, E. Turtle, et al., New frontiers-class uranus orbiter: Exploring the feasibility of achieving multidisciplinary science with a mid-scale mission, Bull. Amer. Astron. Soc. 53 (4) (2021) 323, http://dx.doi.org/10.3847/25c2cfeb.262fe20d.

[30] A.P. Girija, A Systems Framework and Analysis Tool for Rapid Conceptual Design of Aerocapture Missions (Ph.D. Thesis), Purdue University, West Lafayette, IN, 2021, http://dx.doi.org/10.25394/PGS.14903349.v1.

[31] A.P. Girija, S.J. Saikia, J.M. Longuski, J.A. Cutts, AMAT: A python package for rapid conceptual design of aerocapture and atmospheric entry, descent, and landing (EDL) missions in a jupyter environment, J. Open Source Softw. 6 (67) (2021) 3710, http://dx.doi.org/10.21105/joss.03710.

[32] A.P. Girija, Y. Lu, S.J. Saikia, Feasibility and mass-benefit analysis of aerocapture for missions to venus, J. Spacecr. Rockets 57 (1) (2020) 58–73, http://dx.doi.org/10.2514/1.A34529.

[33] K.M. Hughes, Gravity-Assist Trajectories to Venus, Mars, and the Ice Giants: Mission Design with Human and Robotic Applications (Ph.D. Thesis), Purdue University, West Lafayette, IN, 2016.

[34] N.X. Vinh, A. Busemann, R.D. Culp, Hypersonic and Planetary Entry Flight Mechanics, University of Michigan Press, Ann Arbor, MI, 1980, pp. 26–28.

[35] K. Sutton, R.A. Graves Jr., A General Stagnation-Point Convective Heating Equation for Arbitrary Gas Mixtures, Tech. Rep. NASA-TR-R-376, NASA, Washington D. C., 1971, URL https://ntrs.nasa.gov/archive/nasa/casi.ntrs.nasa.gov/19720003329.pdf.

[36] J.A. Samareh, A Multidisciplinary Tool for Systems Analysis of Planetary Entry, Descent, and Landing (SAPE), Tech. Rep. NASA/TM-2009-215950, NASA Langley Research Center, Hampton, VA, 2009, URL https://ntrs.nasa.gov/archive/nasa/casi.ntrs.nasa.gov/20090041828.pdf.

[37] B. Bienstock, D. Atkinson, S. Atreya, P. Mahaffy, K. Baines, M. Wright, M. Wright, A. Stern, P. Steffes, D. Smith, R. Frampton, L. Peltz, S. Sichi, J. Masciarelli, J. Van Cleve, D. Murrow, B. Landin, NASA Vision Mission Neptune Orbiter with Probes, Tech. Rep. Contract No. NNH04CC41C, NASA, 2005.

[38] A.P. Girija, S.J. Saikia, J.M. Longuski, S. Bhaskaran, M.S. Smith, J.A. Cutts, Feasibility and performance analysis of neptune aerocapture using heritage blunt-body aeroshells, J. Spacecr. Rockets 57 (6) (2020) http://dx.doi.org/10.2514/1.A34719.

[39] E.R. Hillje, Entry Flight Aerodynamics from Apollo Mission AS-202, Tech. Rep. NASA TN D-4185, NASA, Washington D. C., October, 1967, URL https://ntrs.nasa.gov/archive/nasa/casi.ntrs.nasa.gov/19670027745.pdf.

[40] D.W. Way, R.W. Powell, A. Chen, A.D. Steltzner, A.M. San Martin, P.D. Burkhart, et al., Mars science laboratory: Entry, descent, and landing system performance, in: 2007 IEEE Aerospace Conference, IEEE, Big Sky, MT, 2007, pp. 1–19, http://dx.doi.org/10.1109/AERO.2007.352821.

[41] C. Cerimele, J. Gamble, A simplified guidance algorithm for lifting aeroassist orbital transfer vehicles, in: 23rd Aerospace Sciences Meeting, Houston, TX, 1985, p. 348, http://dx.doi.org/10.2514/6.1985-348.

[42] E. Roelke, P.D. Hattis, R. Braun, Improved atmospheric estimation for aerocapture guidance, in: 2019 AAS/AIAA Astrodynamics Specialist Conference, Portland, ME, 2019.

[43] J.F. Hamel, J.D. Lafontaine, Improvement to the analytical predictor-corrector guidance algorithm applied to mars aerocapture, J. Guid. Control Dyn. 29 (4) (2006) 1019–1022, http://dx.doi.org/10.2514/1.20126.

[44] B. Starr, C. Westhelle, J. Masciarelli, Aerocapture performance analysis for a neptune-triton exploration mission, in: AIAA Atmospheric Flight Mechanics Conference and Exhibit, AIAA, Providence, RI, 2004, p. 4955, http://dx.doi.org/10.2514/6.2004-4955.

[45] H.L. Justh, A.M. Dwyer Cianciolo, J. Hoffman, G.A. Allen Jr., Uranus Global Reference Atmospheric Model (Uranus-GRAM): User Guide, Tech. Rep. NASA/TM-20210017250, NASA, Huntsville, AL, June, 2021, URL https://ntrs.nasa.gov/api/citations/20210017250/downloads/TM20210017250.pdf.

[46] R.G. Deshmukh, D.A. Spencer, S. Dutta, Investigation of direct force control for aerocapture at neptune, Acta Astronaut. 175 (2020) 375–386, http://dx.doi.org/10.1016/j.actaastro.2020.05.047.

[47] R.G. Deshmukh, System Analysis of a Numerical Predictor-Corrector Aerocapture Guidance Architecture (Ph.D. Thesis), Purdue University, West Lafayette, IN, 2021, http://dx.doi.org/10.25394/PGS.14403542.v1.

[48] R.G. Deshmukh, D.A. Spencer, S. Dutta, Flight control methodologies for neptune aerocapture trajectories, Acta Astronaut. 193 (2022) 255–268, http://dx.doi.org/10.1016/j.actaastro.2022.01.004.

[49] E. Venkatapathy, D. Prabhu, G. Allen, M. Gasch, Thermal protection system to enable ice giant aerocapture mission for delivering both an orbiter and an in situ probe, Bull. AAS 53 (4) (2021) http://dx.doi.org/10.3847/25c2cfeb.0423a253.

[50] R.E. Young, The Galileo probe mission to Jupiter: Science overview, 1998, http://dx.doi.org/10.1029/98JE01051.